scientific reports

Check for updates

OPEN

Metallic ground states of undoped Ti_2O_3 films induced by elongated *c*-axis lattice constant

K. Yoshimatsu[1,2]✉, N. Hasegawa[1], Y. Nambu[3], Y. Ishii[4], Y. Wakabayashi[2,4] & H. Kumigashira[1,2,5]

Ti_2O_3 exhibits unique metal–insulator transition (MIT) at ~ 450 K over a wide temperature range of ~ 150 K. The close relationship between MIT and crystal deformation has been proposed. However, as physical properties are governed by the thermodynamic equilibrium in bulk systems, conducting experimental studies under different lattice deformations remains challenging. Epitaxial thin films can offer high flexibility to accommodate adaptive crystal lattices and provide efficient platforms for investigating the MIT. In this study, we report the synthesis of corundum-type Ti_2O_3 films on various growth temperatures. We found that the metallic ground states appeared in the films grown at low temperatures. The electronic ground states were further investigated by the electronic-structure calculations. Results suggest that the electrical properties of Ti_2O_3 films were governed by the *c*/*a* ratio of the crystal structure, and the absence of the MIT was attributed to the lattice deformation characterized by an elongated *c* lattice constant.

Ti_2O_3 with a corundum-type crystal structure exhibits unique metal–insulator transition (MIT). It is a nonmagnetic insulator with a small bandgap energy of ~ 100 meV[1] at low temperatures, and exhibits transition to metallic states at high temperatures, i.e., ~ 450 K[2–9], which extends over a broad temperature of ~ 150 K. This is indeed unique than most other transition-metal oxide systems. Although the crystal symmetry remains unchanged across the MIT, the *c*/*a* ratio of unit cell changes significantly, thereby suggesting a close relationship between the MIT and lattice deformations[4–9].

The MIT mechanism has been discussed based on experimental and theoretical investigations[1–22]. The most relevant phenomenon to this mechanism is the overlap of a_{1g} and e_g^{π} bands due to the modulations of Ti–Ti distances along the *c*-axis of the crystal lattice[5,8]. Owing to the trigonal distortions in octahedral geometry, the t_{2g} levels in TiO_6 octahedra further split into a_{1g} and e_g^{π} levels. The a_{1g} orbitals between the face-shared TiO_6 octahedra along the *c*-axis are strongly hybridized to form a_{1g} and a_{1g}^* bands with e_g^{π} bands between them. When Ti–Ti bond distances along the *c*-axis are short, the energy splitting between a_{1g} and a_{1g}^* bands becomes large so that the e_g^{π} bands do not overlap with the a_{1g} bands. Furthermore, only the a_{1g} band is completely filled with Ti 3*d* electrons; therefore, Ti_2O_3 acts as an insulator.

The energy diagram describes the electronic structures of Ti_2O_3 revealing the close connection between the MIT and *c*/*a* ratio. The *a* and *c* lattice constants of Ti_2O_3 vary significantly with temperatures, and the *c*/*a* ratio increases from 2.648 at 373 K to 2.701 at 553 K across the MIT[4]. The modulation of Ti 3*d* electron occupations in a_{1g} orbitals associated with a change in the *c*/*a* ratio was revealed from the temperature dependence of linear dichroism in Ti 2*p* X-ray absorption spectra[3,20,21]. However, the band-structure calculations concerned the validity of this simple phenomenological model because a_{1g} and e_g^{π} bands always overlap for typical Ti–Ti distances. A short Ti–Ti distance of less than 2.2 Å is required to form the aforementioned insulating band diagram[14], thereby confirming the importance of electron correlations in Ti_2O_3. Therefore, to understand the mechanism of this MIT better, studies on physical properties of Ti_2O_3 as a function of *c*/*a* ratios are required.

Recently, single-crystalline corundum-type Ti_2O_3 films were synthesized on isostructural α-Al_2O_3 (0001) substrates[23–25], wherein their physical properties were found modulated from those of the bulk systems due to the lattice deformations. The MIT temperature was found in the range of ~ 200–300 K for the films, which is ~ 200 K

[1]Institute of Multidisciplinary Research for Advanced Materials, Tohoku University, Sendai, Miyagi 980-8577, Japan. [2]Materials Research Center for Element Strategy (MCES), Tokyo Institute of Technology, Yokohama 226-8503, Japan. [3]Institute for Materials Research, Tohoku University, Sendai, Miyagi 980-8577, Japan. [4]Department of Physics, Tohoku University, Sendai, Miyagi 980-8578, Japan. [5]Photon Factory, Institute of Materials Structure Science, High Energy Accelerator Research Organization (KEK), 1-1 Oho, Tsukuba 305-0801, Japan. ✉email: kohei.yoshimatsu.c6@tohoku.ac.jp

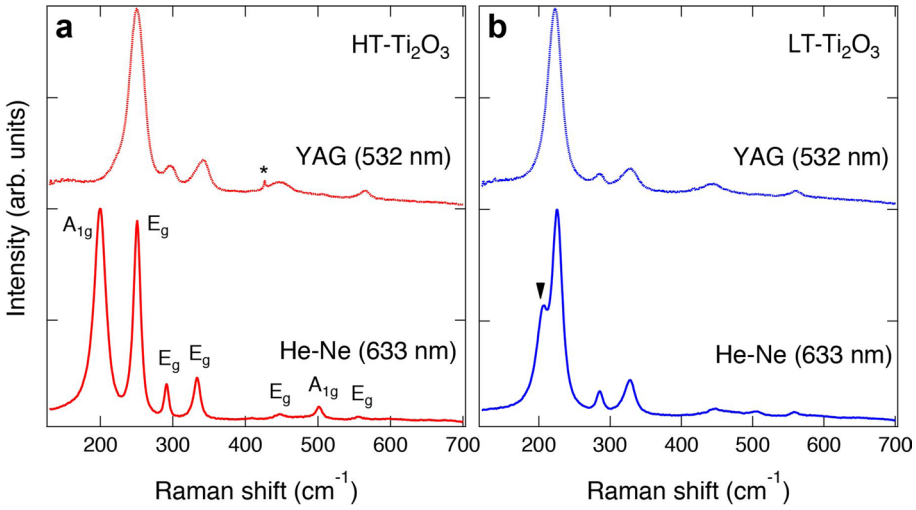

Figure 1. Investigation of corundum-type crystal structure in the Ti_2O_3 films. Raman spectra of (**a**) HT- and (**b**) LT-Ti_2O_3 films measured at RT. The spectra were collected using YAG (dotted lines) and He–Ne (solid lines) lasers. Vibrational modes (A_{1g} or E_g) are indicated in the spectrum of the HT-Ti_2O_3 film recorded using He–Ne laser. The triangle in (**b**) indicates the peak related to the low-frequency A_{1g} mode. The asterisk indicates the peak from the α-Al_2O_3 substrate.

lower than that of the bulk[23,24]. Besides, a significant increase in the *c* lattice constant was detected in the films (at RT $c \sim 13.8$ Å in the films and $c = 13.61$ Å in the bulk). Considering the close relationship between the *c*/*a* ratio and MIT observed in the bulk system, it can be presumed that the suppression of the insulating states in the films is equally related to the lattice deformations. Unfortunately, lattice deformations are not expected in the films grown coherently on α-Al_2O_3 (0001) substrates due to the large lattice mismatch between α-Al_2O_3 and Ti_2O_3 (~8.3%). Furthermore, in contrast to the perovskite-type oxides, corundum-type oxides have the only option of α-Al_2O_3 as an isostructural substrate, which makes it difficult to investigate the physical properties as a function of the *c*/*a* ratio by conventional epitaxial-strain manipulations.

To investigate the relationship between *c*/*a* ratios and MIT in Ti_2O_3, we demonstrate another approach to control the lattice deformation in Ti_2O_3 films, which involves different growth temperatures to manipulate domain sizes and thereby different *c*/*a* ratios. The substrate temperature plays a crucial role in the nucleation of films, and domain sizes vary depending on the growth conditions[26]. In corundum-type oxides such as Ti_2O_3 and V_2O_3, it is known that *a* and *c* lattice constants evolve with the size of nanoparticles[15,27]. Therefore, Ti_2O_3 films grown under different temperatures are expected to render different *a* and *c* lattice constants and electrical properties. In this study, we have grown corundum-type Ti_2O_3 films at high (1000 °C) and low (500 °C) temperatures. The successful synthesis of corundum-type Ti_2O_3 films on α-Al_2O_3 substrates at different temperatures was confirmed by Raman spectroscopy and X-ray diffraction (XRD) experiments. The *c*/*a* ratios at RT were determined as 2.696 and 2.781 for the films grown at high and low temperatures, respectively. Notably, metallic ground states appeared for the film grown under low temperatures, manifesting a large *c*/*a* ratio with domain sizes of the order of 10 nm, whereas MIT was observed in the film grown at high temperatures. We discuss the origin of this MIT behavior in the Ti_2O_3 films by adopting density functional theory (DFT)-based electronic-structure calculations.

Results and discussion

Figure 1 shows the Raman spectra of the high-temperature-Ti_2O_3 (HT-Ti_2O_3) and low-temperature-Ti_2O_3 (LT-Ti_2O_3) films. The Raman spectrum of the HT-Ti_2O_3 film recorded using a He–Ne laser shows seven peaks, which is consistent with previous reports[11–13,24,25]. In corundum-type crystal structures, two A_{1g} and five E_g modes are Raman active following the symmetry considerations[28]. To reveal the vibrational modes in the HT-Ti_2O_3 film, we further performed Raman spectroscopy using another light source of a Nd:$Y_3Al_5O_{12}$ (YAG) laser, as shown in Fig. 1a. Evidently, the lowest-frequency mode was not observed in the spectrum due to the resonant Raman effect reflecting the electronic structures of corundum-type Ti_2O_3[13]. Therefore, the 1st and 2nd low-frequency modes were assigned to the A_{1g} and E_g modes, respectively, which are consistent with the earlier report by Shin et al.[12,13] (see Supplementary Note 1). Our results indicate that both peak structures and resonant Raman effects are good fingerprints to elucidate corundum-type Ti_2O_3[11–13,24,25,29–34].

Similar Raman spectra were obtained for the LT-Ti_2O_3 film, as shown in Fig. 1b, confirming the same crystal structure as that of the HT-Ti_2O_3 film. The Raman spectrum recorded using the He–Ne laser also shows seven peaks, although the peak shapes were slightly different from those of the HT-Ti_2O_3 film. The E_g modes softened, and in contrast, the frequency of the low-frequency A_{1g} mode increased, as shown by the filled triangle in Fig. 1b. Therefore, the A_{1g} and E_g modes at ~230 cm^{-1} were overlapped with each other. These behaviors were also observed in the bulk systems at high temperatures rendering large *c*/*a* ratios[12]. We will discuss the difference in the Raman spectra between the HT- and LT-Ti_2O_3 films later in connection with the transport properties. Nevertheless, the Raman spectrum of the LT-Ti_2O_3 film measured using the YAG laser was in good agreement with that

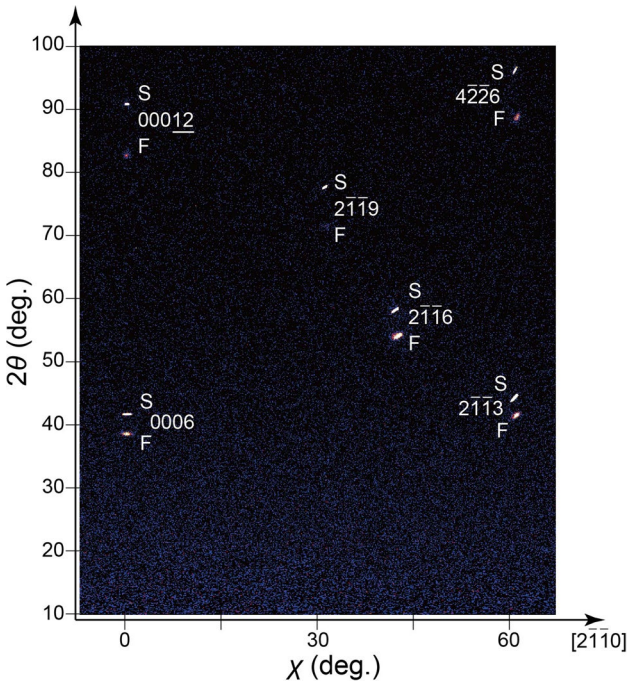

Figure 2. Identical crystal structure for the LT-Ti_2O_3 film and α-Al_2O_3 substrate. 2D XRD contour map of the LT-Ti_2O_3 film on α-Al_2O_3 (0001) substrates. The labels F and S denote the reflections from the LT-Ti_2O_3 film and α-Al_2O_3 substrate, respectively. The tilt angle $\chi = 0°$ corresponds to out-of-plane directions. The azimuthal angle φ is fixed along [2-1-10] direction.

of the HT-Ti_2O_3 film, as shown in Fig. 1b. These results suggest that the LT-Ti_2O_3 film exhibits corundum-type crystal structures and its electronic structures are similar to those in bulk Ti_2O_3 at high temperatures.

Corundum-type crystal structure of the LT-Ti_2O_3 film was further confirmed from the two-dimensional (2D) XRD contour map, as shown in Fig. 2. At the tilt angle $\chi = 0°$, which corresponds to out-of-plane direction, α-Al_2O_3 0006 and 00,012 reflections were detected at $2\theta = \sim 42°$ and 91°, respectively. The reflections from the film were detected at $2\theta = \sim 38°$ and 84° at the tilt angle $\chi = 0°$, which can be assigned to 0006 and 00012 reflections of Ti_2O_3, respectively. All the film reflections were detected at lower 2θ angles than the substrate reflections at the same tilt angle χ. Such pairs of film and substrate reflections observed from the 2D XRD contour maps confirm the identical crystal symmetry of the film and substrate. The 2D XRD contour maps taken along other in-plane directions are shown in Supplementary Fig. 1. These results confirm that the LT-Ti_2O_3 film also exhibits corundum-type crystal structure. Both in-plane and out-of-plane orientations were identical in the LT-Ti_2O_3 film and α-Al_2O_3 substrates.

The detailed lattice constants of the Ti_2O_3 films were determined from the XRD measurements. Figure 3a shows the out-of-plane XRD patterns from the HT- and LT-Ti_2O_3 films. Herein, 0006 and 00012 reflections of the HT-Ti_2O_3 (LT-Ti_2O_3) film were detected at $2\theta = 39.13°$ and 84.11° (38.57° and 82.66°), respectively. The c lattice constant of the HT-Ti_2O_3 (LT-Ti_2O_3) film was 13.80 Å (14.00 Å), which is larger than that of the bulk Ti_2O_3 at RT ($c = 13.61$ Å)[4]. The possible origin of the increased c lattice constants can be smaller domain sizes, which will be discussed later. The in-plane lattice constants were determined from the reciprocal space maps. Figure 3b,c shows the reciprocal space maps of the HT- and LT-Ti_2O_3 films around the α-Al_2O_3 10-1$\underline{1}\underline{0}$ reciprocal point, respectively. From the reciprocal point of Ti_2O_3 10-1$\underline{1}\underline{0}$, a lattice constant of the HT-Ti_2O_3 (LT-Ti_2O_3) film was found 5.119 Å (5.034 Å). The resultant c/a ratio of the HT-Ti_2O_3 (LT-Ti_2O_3) film was 2.696 (2.781), which is much larger than that of the bulk Ti_2O_3 ($c/a = 2.639$). Note that the c/a ratio of the LT-Ti_2O_3 film is also much larger than that of typical corundum-type oxides such as α-Al_2O_3 ($c/a = 2.732$ where $a = 4.759$ Å and $c = 12.99$ Å), but relatively smaller than that of another corundum-type oxide V_2O_3 ($c/a = 2.828$ where $a = 4.9717$ Å and $c = 14.005$ Å)[35].

The different growth temperatures also significantly affected the surface morphologies of the films. As shown in Fig. 4a, the atomic force microscope (AFM) image of the HT-Ti_2O_3 film reflected a trace of spiral growths[36], which was also reported previously[23]. The in-plane size of the spirals was ~ 0.5 μm. In contrast, the LT-Ti_2O_3 film did not exhibit such spiral growths in the AFM image as shown in Fig. 4b. Instead, smaller grains of less than 50 nm were detected at the surface, which can be attributed to the reduced migration energies during the low-temperature growth process[26]. Out-of-plane grain sizes were roughly estimated from the out-of-plane XRD patterns (See Supplementary Note 2). The broad peaks in the LT-Ti_2O_3 film, as shown in Fig. 3a, also suggested small grain sizes. Grain sizes of the LT-Ti_2O_3 film were estimated as 23 nm from the Scherrer equation, which is comparable to the estimation from the AFM image (See Supplementary Note 2 for the detailed analyses). In corundum-type Ti_2O_3 and V_2O_3 nanoparticles, it was reported that lattice constants evolved greatly with the particle sizes[15,27]. In the case of Ti_2O_3, the c (a) lattice constant becomes longer (shorter) as the grain size

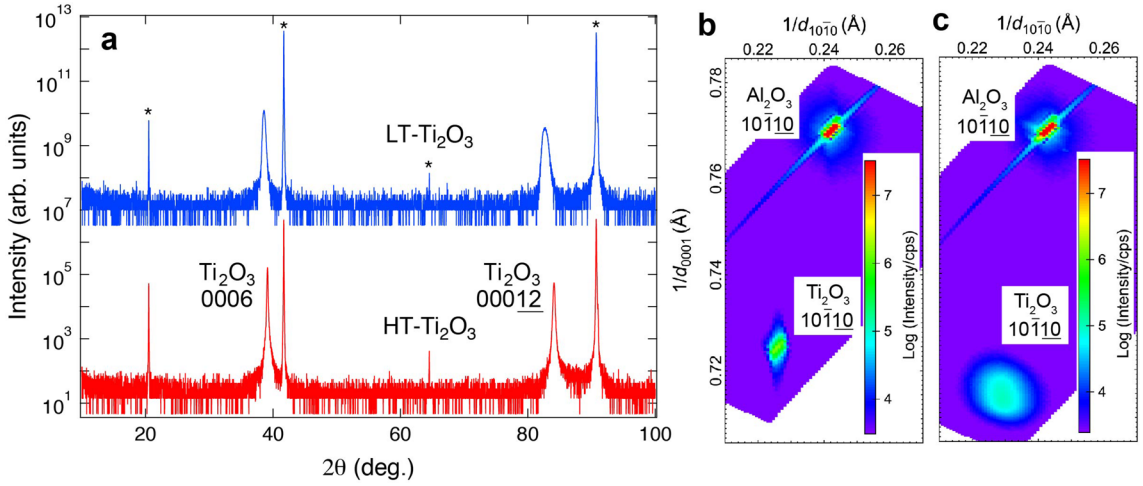

Figure 3. Determination of in-plane and out-of-plane lattice constants of the Ti_2O_3 films. (**a**) Out-of-plane XRD patterns for the HT- and LT-Ti_2O_3 films. The asterisks indicate the reflection coming from α-Al_2O_3 (0001) substrates. Reciprocal space maps around α-Al_2O_3 10-1$\underline{1}$0 reciprocal points in the cases of the (**b**) HT- and (**c**) LT-Ti_2O_3 films.

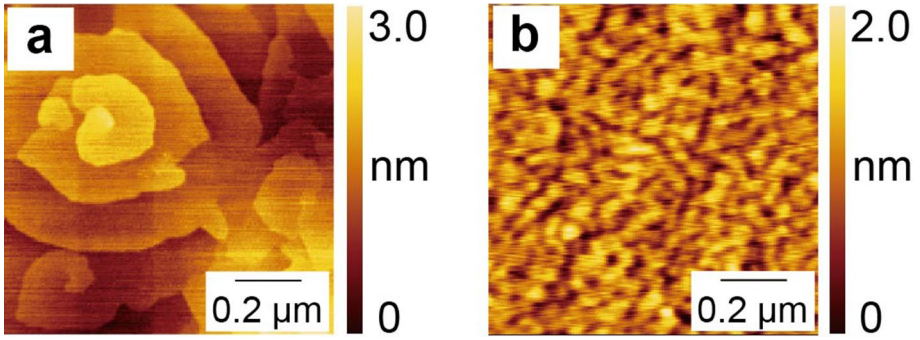

Figure 4. Surface morphology of the Ti_2O_3 films. AFM images of the (**a**) HT- and (**b**) LT-Ti_2O_3 films.

decreases, resulting in an increased *c*/*a* ratio for the nanoparticles[15]. Considering the larger size (~ 1 mm scale) of the Ti_2O_3 single crystal, the negative correlation between the domain size and *c*/*a* ratio is plausible in the films.

It is well established that the *c*/*a* ratio is strongly related to the MIT in the bulk Ti_2O_3[4]. To elucidate the relationship between the MIT and *c*/*a* ratios in the Ti_2O_3 films, we performed temperature-dependent resistivity measurements for the HT- and LT-Ti_2O_3 films, as shown in Fig. 5a. For the HT-Ti_2O_3 film, the resistivity at 2 K was ~ 10 mΩ cm. The resistivity gradually decreased with increasing temperatures and the broad MIT appeared at 200–300 K accompanying a substantial change in the resistivity. Even beyond the MIT, dρ/dT remained negative up to 400 K (ρ and T denote resistivity and temperature, respectively). Such resistivity behaviors suggest the suppression of insulating states in Ti_2O_3 films in comparison with bulk, which is also consistent with the previous reports[23,24]. In bulk, the resistivity at ~ 10 K is more than 10^2 Ω cm[2,3], which is four orders of magnitude larger than that of the HT-Ti_2O_3 film. In addition, the MIT temperature in bulk is ~ 450 K, which is ~ 200 K higher than that of the film[23,24].

Suppression of the insulating states is further examined in the LT-Ti_2O_3 film that show a completely different resistivity curve, as shown in Fig. 5a. The MIT was not observed and metallic conductivity (dρ/dT > 0) appeared until ~ 50 K. However, at temperatures < 50 K, a slight upturn of the resistivity curve was noticed, suggesting a trap of conductive carriers in defects at low temperatures, which can be related to the poor crystallinity of the LT-Ti_2O_3 film (See Supplementary Fig. 2). In bulk $(Ti_{1-x}V_x)_2O_3$, resistivity of low-temperature insulating phases decrease drastically with V doping, but another phase transition was detected at high-temperature regions (~ 450 K)[2]. To eliminate the possible phase transition in the LT-Ti_2O_3 film, we further performed high-temperature resistivity measurements, as shown in the inset of Fig. 5a. The metallic conductivity continued up to 600 K with a linear ρ–T relationship. We note that metallic conductivity first appears at ~ 500 K for the HT-Ti_2O_3 film[23], but it is never observed for a bulk system up to 575 K[2,3].

The electric properties were further investigated from Hall-effect measurements. The clear linear dependence of the Hall resistance on the magnetic field was observed for both films (see Supplementary Fig. 3). We plot the resultant inverse Hall coefficient ($1/R_H$) in Fig. 5b as a function of temperature. The positive $1/R_H$ indicates the hole-carrier conduction of both films, which is consistent with the previous reports[1,37]. The $1/R_H$ became smaller

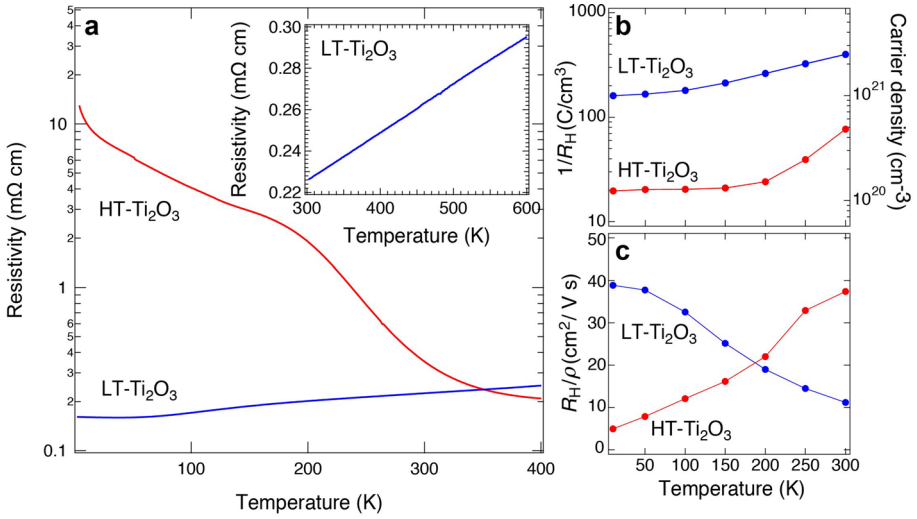

Figure 5. Electric properties of the Ti_2O_3 films. (**a**) Temperature dependence of resistivity for the HT- and LT-Ti_2O_3 films. The inset shows temperature dependence of resistivity for the LT-Ti_2O_3 film above RT. Temperature dependence of the (**b**) inverse Hall coefficient $1/R_H$ and (**c**) Hall mobility R_H/ρ of the HT- and LT-Ti_2O_3 films.

with decreasing temperature for both films. In particular, the $1/R_H$ of the HT-Ti_2O_3 film drastically decreased in the temperature range from 300 to 200 K, reflecting the occurrence of MIT. Assuming the single-band model, we estimated the carrier densities of the films as indicated by the scale on the right axis in Fig. 5b. The carrier densities at 300 K were 4.8×10^{20} cm^{-3} and 2.5×10^{21} cm^{-3} for the HT- and LT-Ti_2O_3 films, respectively. The temperature dependence of the Hall mobility (R_H/ρ) was also plotted in Fig. 5c. The R_H/ρ decreased to be < 10 cm^2/V s in low temperatures for the HT-Ti_2O_3 film. In contrast, the R_H/ρ was as high as 10–40 cm^2/V s for the LT-Ti_2O_3 film in the whole temperatures, supporting the metallic ground states of the LT-Ti_2O_3 film.

The metallic states of the LT-Ti_2O_3 film are further supported by Raman spectroscopy (Fig. 1). Shin et al. reported that the low-frequency A_{1g} mode is an excellent indicator of the electrical behaviors of Ti_2O_3[12,13]. The A_{1g} vibrational modes correspond to breathing against one another for the Ti atom pairs along the *c*-axis. Simultaneously, oxygen atoms forming triangles between each Ti pair are moving in and out alternately with respect to each other. In the low-frequency A_{1g} mode, oxygen atoms move out when the Ti atoms move in, so that the screening effect of the oxygens becomes lowest, and the modulation of the trigonal component to the crystalline field rises to its largest value. In a phenomenological model, the intensity of Raman mode is related to the polarizability of the electron cloud. As shown in Fig. 1a, the Raman spectrum of the HT-Ti_2O_3 film collected using the He–Ne laser showed the strongest intensity for the low-frequency A_{1g} mode, which is consistent with the phenomenological model. In contrast, the intensity of the A_{1g} mode was strongly suppressed in the LT-Ti_2O_3 film due to conduction-carrier screening of the electric field caused by the electron cloud motions. Since the screening effect from the oxygens is weakest in the low-frequency A_{1g} mode, its intensity gets most affected. Therefore, the strong suppression of the low-frequency A_{1g} mode provides further evidence for the metallic conductivity in the LT-Ti_2O_3 film.

One might suspect that different carrier densities (4.8×10^{20} cm^{-3} for the HT-Ti_2O_3 film and 2.5×10^{21} cm^{-3} for the LT-Ti_2O_3 film at 300 K) are caused by extrinsic effects such as oxygen non-stoichiometry. However, it is unlikely in the present case. In Ti_2O_3, the atomic density of Ti in the crystal lattice is calculated to be 3.8×10^{22} cm^{-3}. The carrier densities correspond to be 1.3 and 6.6% holes /Ti for the HT- and LT-Ti_2O_3 films, respectively. Meanwhile, Andersson et al. revealed that the corundum-type Ti_2O_3 phase was only stable with the oxygen non-stoichiometry of less than 1%, corresponding to the chemical formula of $Ti_2O_{2.98}$–$Ti_2O_{3.02}$[38]. These results suggest that the carrier density of the LT-Ti_2O_3 film is not explained by the oxygen non-stoichiometry.

The plausible scenario to explain different hole-carrier densities between the HT- and LT-Ti_2O_3 films is the intrinsic holes whose densities are varied by the *c*/*a* ratio. Chang et al. revealed the change of the Ti 3*d* electron occupation in the a_{1g} and e_g^{π} orbitals by the *c*/*a* ratio[3]. We note that the *c*/*a* ratio directly corresponds to the degree of the trigonal distortion in TiO_6 octahedra and the distance of Ti–Ti pair along the *c*-axis. When the *c*/*a* ratio was small enough, the Ti 3*d* electrons completely filled the most stable a_{1g} orbital, resulting in the formation of 100% $a_{1g}a_{1g}$ singlet state in the Ti–Ti pair. With increasing the *c*/*a* ratio, the occupation in the a_{1g} orbital systematically decreased. According to Ref. 3, the $a_{1g}a_{1g}$ singlet state was reduced to be 49% at 575 K (*c*/*a* = 2.70). The reduction in the $a_{1g}a_{1g}$ singlet state is responsible for increasing the hole carriers in the a_{1g} bands. Moreover, the rest of the Ti 3*d* electrons is partially filled with the e_g^{π} orbital that expands in the *a*–*b* plane. The partially-filled e_g^{π} orbital forms conducting paths to the neighboring Ti–Ti pairs, resulting in the large hole-carrier densities and metallic conductivity in the LT-Ti_2O_3 film.

Next, to reveal the origin of different electronic states in the films and bulk materials, we performed DFT + *U* calculations using the Quantum ESPESSO simulation software[39,40]. Since insulating ground states were not

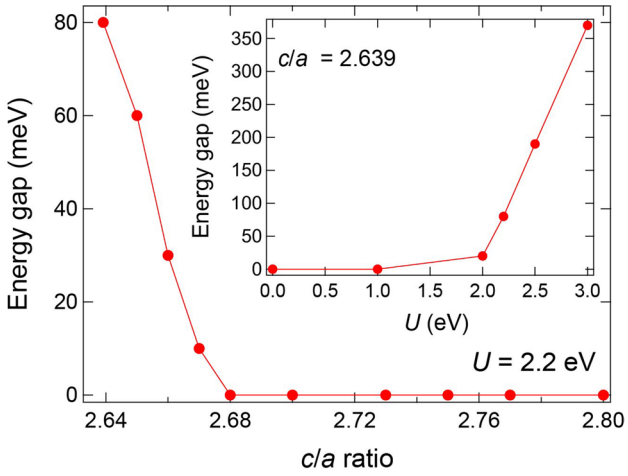

Figure 6. Lattice deformation induced MIT from DFT calculation. Plots of the energy gap at E_F from DFT + U calculations with $U = 2.2$ eV as a function of c/a ratios. The inset shows plots of the energy gap at E_F in bulk Ti_2O_3 ($c/a = 2.639$) as a function of U values.

reproduced in Ti_2O_3 by DFT calculations[14], we first estimated adequate Hubbard U parameter to reproduce the experimental energy gap. The inset of Fig. 6 shows the energy gap at the Fermi level (E_F) of Ti_2O_3 with a c/a ratio of 2.639 (bulk value at RT) as a function of U values. When U was not introduced in calculations, the energy gap was 0 meV, corresponding to the metallic ground states. The energy gap emerged when U was larger than 2.0 eV, and it gradually increased with an increase in U values. For example, the energy gaps at $U = 2.2$, 2.5, and 3.0 eV were 80, 190, and 370 meV, respectively. Considering the experimental energy gap of ~ 100 meV[1], we set $U = 2.2$ eV for the subsequent calculations (See Supplementary Fig. 4 for the DOS of Ti_2O_3).

The MIT derived from the lattice deformations was demonstrated by the DFT + U calculations. Figure 6 shows the energy gap at E_F as a function of c/a ratios at $U = 2.2$ eV. The energy gap was 80 meV at $c/a = 2.639$, and it became narrower with an increase in the c/a ratio. Eventually, the gap closed at a critical c/a ratio of 2.68, whereas the metallic ground states continued to be stable up to a c/a ratio of 2.8. The critical c/a ratio of 2.68 is in good agreement with the experimental results[4]. In bulk materials, the c/a ratio reaches 2.68 at ~ 470 K in the middle of the broad MIT. Considering the c/a ratios of the HT-Ti_2O_3 (2.696) and LT-Ti_2O_3 (2.781) films, both types of films were in metallic regions at RT, corroborating the ρ–T curves provided in Fig. 5a.

We will discuss the plausible origin behind the occurrence of the MIT in the HT-Ti_2O_3 film and the absence of the MIT in the LT-Ti_2O_3 film at low temperatures. The a and c lattice constants should be modulated as a function of temperature due to the thermal expansion. To experimentally estimate thermal expansion coefficients (α) of the Ti_2O_3 films, we performed the temperature-dependent XRD measurements (see Supplementary Figs. 6–8). The α along the c-axis (α_c) and a-axis (α_a) were estimated to be $\alpha_c = 1.86 \pm 0.17 \times 10^{-5}$ K^{-1} and $\alpha_a = 2.10 \pm 2.97 \times 10^{-6}$ K^{-1} for the HT-Ti_2O_3 film and to be $\alpha_c = 1.70 \pm 0.11 \times 10^{-5}$ K^{-1} and $\alpha_a = -0.37 \pm 3.32 \times 10^{-6}$ K^{-1} for the LT-Ti_2O_3 film. The relative errors of the α_a look large, which originates temperature-independent a lattice constants. We also referred to the α of bulk Ti_2O_3 that was estimated to be $\alpha_c = 3.263 \times 10^{-5}$ K^{-1} and $\alpha_a = -1.088 \times 10^{-6}$ K^{-1} using previous results (see Supplementary Fig. 9)[4]. We found that the α_c of the films was approximately half of the α_c of the bulk specimen. We utilized the α determined from the present experiments and the bulk reference and then obtained the c/a ratios of the films below RT by the linear extrapolation of the values in the high-temperature metallic region to low temperatures (See Supplementary Fig. 10). In the HT-Ti_2O_3 film, the c/a ratio reached the critical value of 2.68 at ~ 150 K using the α of the bulk reference and at ~ 50 K using the experimentally determined α. Although these critical MIT temperatures are much lower than that revealed from the temperature dependence of resistivity (~ 250 K in Fig. 5a), the results qualitatively demonstrate that the MIT in the HT-Ti_2O_3 film is due to the temperature dependence of the crystal deformation. In contrast, the LT-Ti_2O_3 film did not reach the critical c/a ratio of 2.68 even at the lowest temperature limit. The estimated c/a ratio at 2 K was larger than 2.754, where the metallic states appeared in the DFT calculations and in experiments for the bulk materials. These results suggest that the electrical properties of both HT- and LT-Ti_2O_3 films can be explained by the c/a ratio as in the bulk systems. Absence of the MIT in the LT-Ti_2O_3 film can be attributed to the elongated c lattice constant (at RT $c = 14.00$ Å in the film and $c = 13.61$ Å in the bulk) caused by the nano-sized domains.

We presume that treatment of the empirical parameter U is responsible for the quantitative discrepancies in the critical temperatures between the experiment and the calculation. In the DFT + U calculations, the critical c/a ratio had a positive correlation with U. Moreover, the energy gap quite sensitively depended on U, as shown in Fig. 6. In this study, we merely selected $U = 2.2$ eV to reproduce the energy gap (~ 100 meV) for bulk Ti_2O_3. Therefore, it is quite difficult to determine the critical c/a ratio from the DFT + U calculations quantitatively at the moment, although the close relationship between c/a ratios and MIT in Ti_2O_3 is clearly demonstrated on the qualitative level. To resolve the quantitative discrepancies between the experiments and calculations, further experimental studies to determine the energy gap of bulk Ti_2O_3 precisely and more accurate theoretical studies would be required.

Herein, we have grown Ti_2O_3 films on α-Al_2O_3 (0001) substrates at high and low temperatures to control domain sizes and c/a ratios of the structure. Successful synthesis of films exhibiting corundum-type crystal structure in both conditions was confirmed by Raman spectroscopy and XRD measurements. The c/a ratios at RT were significantly different in the HT-Ti_2O_3 (2.696) and LT-Ti_2O_3 (2.781) films. The HT-Ti_2O_3 film showed the broad MIT at ~ 200–300 K, which was ~ 200 K lower than that of the bulk. However, the LT-Ti_2O_3 film exhibited metallic conductivity and did not show any MIT up to 600 K. The DFT + U calculations predicted the critical c/a ratio of 2.68 to induce the MIT. The detailed analyses revealed that the observed electrical properties of the Ti_2O_3 films can be explained by the critical c/a ratio and anisotropic thermal expansion coefficients. These results suggest that the electrical properties of Ti_2O_3 films are also governed by the c/a ratio of the structure and the absence of the MIT in the LT-Ti_2O_3 film is due to the lattice deformations characterized by an increased c lattice constant leading to an enhanced $c/a = 2.781$ at RT.

Methods

Thin-film growth. Ti_2O_3 films were grown on α-Al_2O_3 (0001) substrates using the pulsed-laser deposition (PLD) method. Polycrystalline ceramics of TiO (3 N purity, purchased from Toshima Manufacturing Co., Ltd.) were used as the PLD target. A KrF excimer laser (0.8 J/cm^2, 5 Hz) was used for target ablations. The substrate temperature and oxygen partial pressure were set 1000 °C and 1.5×10^{-6} Torr, respectively, for the production of the HT-Ti_2O_3 film, whereas those for the preparation of the LT-Ti_2O_3 film with single-phases were 500 °C and 5.0×10^{-7} Torr, respectively. Notably, when the temperature was set between 500 and 1000 °C, another superconducting-titanate phase was stabilized and consequently, single-phase corundum-type Ti_2O_3 films were not obtained (See Supplementary Figs. 11–14). At the end of the growth process, the oxygen flow to the PLD chamber was stopped immediately and films were quenched to RT to avoid the occurrence of additional oxidations[23,41]. Film thickness (~ 100 nm) was measured using a stylus-type profiler.

Thin-film characterizations. Crystal structures of the films were revealed by Raman spectroscopy and XRD measurements conducted at RT. Raman spectra were acquired using a LabRAM HR-800 (Horiba) equipped with YAG ($\lambda = 532$ nm) and He–Ne ($\lambda = 633$ nm) lasers. The laser incident and Raman scattering directions were parallel to the c-axis. The polarization vector of the lasers was set parallel to the Ti_2O_3 [10-10] direction. XRD patterns and contour maps were measured using the Cu–Kα_1 radiation available in a SmartLab 9 kW diffractometer (Rigaku). Surface morphology was examined via AFM. Temperature dependence of resistivity was measured by implementing a standard four-probe method using PPMS (Quantum Design) at low temperatures ($2 \le T \le 400$ K) and PPHL-800 (Pascal) at high temperatures ($300 \le T \le 600$ K). Au electrodes were deposited by the sputtering method. Ohmic contacts between the films and electrodes were confirmed from the two probe I–V measurements at RT. Hall-effect measurements were carried out in a Hall-bar geometry using PPMS.

Electronic structure calculations. DFT calculations were performed using the Quantum ESPRESSO simulation software[39,40]. Ultrasoft pseudopotentials were used, wherein atomic Ti 3*s*, 3*p*, 3*d*, and 4*s*, O 2*s*, and 2*p* levels were included as valence-band states. The Perdew–Burke–Ernzerhof generalized gradient approximation (PBE-GGA) function was utilized for the exchange–correlation potentials[42]. The kinetic energy (charge density) cut-off was set as 60 Ry (600 Ry). Ti and O positions were optimized by a structural relaxation routine implementing Monkhorst–Pack scheme with a $6 \times 6 \times 6$ k-mesh in self-consistent calculations[43]. Accuracy in total energy after the convergence of the self-consistent calculations was less than 10^{-10} Ry. After the structural optimization, the density of states (DOS) was calculated in non-self-consistent fields using a denser $12 \times 12 \times 12$ k-mesh. The tetrahedron method was applied to integrate the DOS in the Brillouin zone[44]. Further computing details are described in Supplementary Methods.

Data availability

The data that support the findings of this study are available from the corresponding author upon reasonable request.

Received: 15 September 2020; Accepted: 4 December 2020
Published online: 17 December 2020

References

1. Honig, J. M. & Reed, T. B. Electrical properties of Ti_2O_3 single crystals. *Phys. Rev.* **174**, 1020–1026 (1968).
2. Uchida, M., Fujioka, J., Onose, Y. & Tokura, Y. Charge dynamics in thermally and doping induced insulator–metal transitions of $(Ti_{1-x}V_x)_2O_3$. *Phys. Rev. Lett.* **101**, 066406 (2008).
3. Chang, C. F. *et al.* c-Axis dimer and its electronic break up: the insulator-to-metal transition in Ti_2O_3. *Phys. Rev. X* **8**, 021004 (2018).
4. Capponi, J. J., Marezio, M., Dumas, J. & Schlenker, C. Lattice parameters variation with temperature of Ti_2O_3 and $(Ti_{0.98}V_{0.02})_2O_3$ from single crystal x-ray data. *Solid State Commun.* **20**, 893–896 (1976).
5. Van Zandt, L. L., Honig, J. M. & Goodenough, J. B. Resistivity and magnetic order in Ti_2O_3. *J. Appl. Phys.* **39**, 594–595 (1968).
6. Honig, J. M. Nature of the electrical transition in Ti_2O_3. *Rev. Mod. Phys.* **40**, 748–751 (1968).
7. Chandrashekhar, G. V., Choi, Q. W., Moyo, J. & Honig, J. M. The electrical transition in V-doped Ti_2O_3. *Mater. Res. Bull.* **5**, 999–1007 (1970).
8. Zeiger, H. J. Unified model of the insulator–metal transition in Ti_2O_3 and the high temperature transitions in V_2O_3. *Phys. Rev. B* **11**, 5132–5144 (1975).
9. Rao, C. N. R., Loehman, R. E. & Honig, J. M. Crystallographic study of the transition in Ti_2O_3. *Phys. Lett.* **27**, 271–272 (1968).
10. Morin, F. J. Oxides which show a metal-to-insulator transition at the Neel temperature. *Phys. Rev. Lett.* **3**, 34–36 (1959).
11. Mooradian, A. & Raccah, P. M. Raman study of the semiconductor–metal transition in Ti_2O_3. *Phys. Rev. B* **3**, 4253–4256 (1971).
12. Shin, S. H., Aggarwal, R. L., Lax, B. & Honig, J. M. Raman scattering in Ti_2O_3–V_2O_3 alloys. *Phys. Rev. B* **9**, 583–590 (1974).

13. Shin, S. H., Pollak, F. H., Halpern, T. & Raccah, P. M. Resonance Raman scattering in Ti_2O_3 in the range 1.8–2.7 eV. *Solid State Commun.* **16**, 687–690 (1975).
14. Mattheiss, L. F. Electronic structure of rhombohedral Ti_2O_3. *J. Phys. Condens. Mater.* **8**, 5987 (1996).
15. Tsujimoto, Y., Matsushita, Y., Yu, S., Yamaura, K. & Uchikoshi, T. Size dependence of structural, magnetic, and electrical properties in corundum-type Ti_2O_3 nanoparticles showing insulator–metal transition. *J. Asian Ceram. Soc.* **3**, 325–333 (2015).
16. Guo, Y., Clark, S. J. & Robertson, J. Electronic and magnetic properties of Ti_2O_3, Cr_2O_3, and Fe_2O_3 calculated by the screened exchange hybrid density functional. *J. Phys. Condens. Mater.* **24**, 325504 (2012).
17. Iori, F., Gatti, M. & Rubio, A. Role of nonlocal exchange in the electronic structure of correlated oxides. *Phys. Rev. B* **85**, 115129 (2012).
18. Poteryaev, A. I., Lichtenstein, A. I. & Kotliar, G. Nonlocal coulomb interactions and metal–insulator transition in Ti_2O_3: a cluster LDA + DMFT approach. *Phys. Rev. Lett.* **93**, 086401 (2004).
19. Tanaka, A. A new scenario on the metal–insulator transition in VO_2. *J. Phys. Soc. Jpn.* **72**, 2433–2436 (2003).
20. Sato, H. *et al.* Ti 3*d* orbital change across metal–insulator transition in Ti_2O_3: polarization-dependent soft x-ray absorption spectroscopy at Ti 2*p* edge. *J. Phys. Soc. Jpn.* **75**, 053702 (2006).
21. Tanaka, A. On the metal–insulator transitions in VO_2 and Ti_2O_3 from a unified viewpoint. *J. Phys. Soc. Jpn.* **73**, 152–162 (2004).
22. Smith, K. E. & Henrich, V. E. Bulk band dispersion in Ti_2O_3 and V_2O_3. *Phys. Rev. B* **38**, 5965–5975 (1988).
23. Yoshimatsu, K., Kurokawa, H., Horiba, K., Kumigashira, H. & Ohtomo, A. Large anisotropy in conductivity of Ti_2O_3 films. *APL Mater.* **6**, 101101 (2018).
24. Li, Y. *et al.* Observation of superconductivity in structure-selected Ti_2O_3 thin films. *npg Asia Mater.* **10**, 522–532 (2018).
25. Shvets, P. V. *et al.* Suppression of the metal–insulator transition in magnetron sputtered Ti_2O_3 films. *Thin Solid Films* **694**, 137642 (2020).
26. Ohring, M. *Materials Science of Thin Films Deposition and Structure* (Academic Press, Cambridge, 2002) (**978-0-12-524975-1**).
27. Ishiwata, Y. *et al.* Spontaneous uniaxial strain and disappearance of the metal–insulator transition in monodisperse V_2O_3 nanocrystals. *Phys. Rev. B* **86**, 035449 (2012).
28. Porto, S. P. S. & Krishnan, R. S. Raman effect of corundum. *J. Chem. Phys.* **47**, 1009–1012 (1967).
29. Balachandran, U. & Eror, N. G. Raman spectra of titanium dioxide. *J. Solid State Chem.* **42**, 276–282 (1982).
30. Watanabe, M. & Ueno, W. Raman study of order-disorder transition of bipolarons in Ti_4O_7. *Phys. Stat. Sol. (c)* **3**, 3456–3459 (2006).
31. Li, X. *et al.* Magneli phase Ti_4O_7 electrode for oxygen reduction reaction and its implication for zinc air rechargeable batteries. *Electrochim. Acta* **55**, 5891–5898 (2010).
32. Wu, Y., Zhang, Q., Wu, X., Qin, S. & Liu, J. High pressure structural study of β-Ti_3O_5: X-ray diffraction and Raman spectroscopy. *J. Solid State Chem.* **192**, 356–359 (2012).
33. Ould-Hamouda, A., Tokoro, H., Ohkoshi, S.-I. & Freysz, E. Single-shot time resolved study of the photo-reversible phase transition induced in flakes of Ti_3O_5 nanoparticles at room temperature. *Chem. Phys. Lett.* **608**, 106–112 (2014).
34. Wang, M. *et al.* Phase evolution and formation of λ phase in Ti_3O_5 induced by magnesium doping. *J. Alloys Compd.* **774**, 1189–1194 (2019).
35. McWhan, D. B., Rice, T. M. & Remeika, J. P. Mott transition in Cr-doped V_2O_3. *Phys. Rev. Lett.* **23**, 1384 (1969).
36. Sunagawa, I., Narita, K., Bennema, P. & Van Der Hoek, B. Observation and interpretation of eccentric growth spirals. *J. Cryst. Growth* **42**, 121–126 (1977).
37. Yahia, J. & Frederikse, H. P. R. Electrical conduction in *p*-type titanium sesquioxide. *Phys. Rev.* **123**, 1257 (1961).
38. Andersson, S., Collén, B. & Kuylenstierna, U. & Magnéli, phase analysis studies on the titanium-oxygen system. *Acta Chem. Scand.* **11**, 1641 (1957).
39. Giannozzi, P. *et al.* Quantum ESPRESSO: a modular and open-source software project for quantum simulations of materials. *J. Phys. Condens. Mater.* **21**, 395502 (2009).
40. Giannozzi, P. *et al.* Advanced capabilities for materials modeling with quantum ESPRESSO. *J. Phys. Condens. Mater.* **29**, 465901 (2017).
41. Yoshimatsu, K., Sakata, O. & Ohtomo, A. Superconductivity in Ti_4O_7 and γ-Ti_3O_5 films. *Sci. Rep.* **7**, 12544 (2017).
42. Perdew, J. P., Burke, K. & Ernzerhof, M. Generalized gradient approximation made simple. *Phys. Rev. Lett.* **77**, 3865–3868 (1996).
43. Monkhorst, H. J. & Pack, J. D. Special points for brillouin-zone integrations. *Phys. Rev. B* **13**, 5188–5192 (1976).
44. Blöchl, P. E., Jepsen, O. & Andersen, O. K. Improved tetrahedron method for brillouin-zone integrations. *Phys. Rev. B Condens. Matter.* **49**, 16223–16233 (1994).

Acknowledgements

This work was partly supported by MEXT Elements Strategy Initiative to Form Core Research Center (JPMXP0112101001), a Grant-in-Aid for Scientific Research (Nos. 19H02588, 20K20887, and 17H06137) from the Japan Society for the Promotion of Science Foundation, CREST (JPMJCR18T1) from the Japan Science and Technology Agency (JST), and Asahi Glass Foundation, Futaba Foundation, Nagamori Foundation, and Nippon Sheet Glass Foundation for Materials Science and Engineering. We greatly thank R. Kumashiro and K. Saitoh in common equipment room of WPI in Tohoku University for the film-thickness measurements, Raman spectroscopy, and XRD measurements. We would like to thank Prof. M. Mitsuishi for AFM measurements in CAF of IMRAM. We also would like to thank Editage (www.editage.com) for English language editing.

Author contributions

K.Y. and N.H. grew the films and investigated their structural and electrical properties. K.Y. performed DFT calculations. Y.N. contributed to the resistivity measurements using PPMS. Y. I. and Y. W contributed to the temperature dependence of the XRD measurements. K.Y. wrote the manuscript under the guidance of H.K. H.K. supervised the project. All authors approved the manuscript.

Competing interests

The authors declare no competing interests.

Additional information

Supplementary Information The online version contains supplementary material available at https://doi.org/10.1038/s41598-020-79182-5.

Correspondence and requests for materials should be addressed to K.Y.

Reprints and permissions information is available at www.nature.com/reprints.